www.advenergymat.de

Doping-Induced Viscoelasticity in PbTe Thermoelectric Inks for 3D Printing of Power-Generating Tubes

Jungsoo Lee, Seungjun Choo, Hyejin Ju, Jaehyung Hong, Seong Eun Yang, Fredrick Kim, Da Hwi Gu, Jeongin Jang, Gyeonghun Kim, Sangjoon Ahn, Ji Eun Lee, Sung Youb Kim,* Han Gi Chae,* and Jae Sung Son*

Thermoelectric (TE) technologies offer promising means to enhance fossil energy efficiencies by generating electricity from waste heat from industrial or automobile exhaust gases. For these applications, thermoelectric modules should be designed from the perspective of system integration for efficient heat transfer, system simplification, and low processing cost. However, typical thermoelectric modules manufactured by traditional processes do not fulfil such requirements, especially for exhaust pipes. Hence, a 3D-printing method for PbTe thermoelectric materials is reported to design high-performance power-generating TE tubes. The electronic doping-induced surface charges in PbTe particles are shown to significantly improve the viscoelasticities of inks without additives, thereby enabling precise shape and dimension engineering of 3D bulk PbTe with figures of merit of 1.4 for p-type and 1.2 for n-type materials. The performance of the power-generating TE tube fabricated from 3D-printed PbTe tubes is demonstrated experimentally and computationally as an effective strategy to design system-adaptive high-performance thermoelectric generators.

J. Lee, S. Choo, H. Ju, S. E. Yang, F. Kim, D. H. Gu, Prof. H. G. Chae, Prof. J. S. Son

Department of Materials Science and Engineering

Ulsan National Institute of Science and Technology (UNIST)

Ulsan 44919, Republic of Korea

E-mail: sykim@unist.ac.kr; hgchae@unist.ac.kr; jsson@unist.ac.kr

Dr. J. Hong, Prof. S. Y. Kim

Department of Mechanical Engineering

Ulsan National Institute of Science and Technology (UNIST)

Ulsan 44919, Republic of Korea

Energy Conversion Research Center

Korea Electrotechnology Research Institute

Changwon 51543, Republic of Korea

G. Kim, Prof. S. Ahn

Department of Nuclear Engineering

Ulsan National Institute of Science and Technology (UNIST)

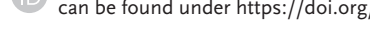
Ulsan 44919, Republic of Korea

Prof. J. E. Lee

School of Chemical Engineering

Chonnam National University

Gwangju 61186, Republic of Korea



The ORCID identification number(s) for the author(s) of this article can be found under https://doi.org/10.1002/aenm.202100190.

DOI: 10.1002/aenm.202100190

1. Introduction

Global energy demand has increased significantly due to the increased global population and improving living standards in developing countries. Given that more than 80% of the current global energy consumption is enabled by fossil fuel sources, renewable energy sources such as the sun, wind, and biomass can be considered as potential solutions to ensure the sustainability of electricity supply. Another potential source of power is heat energy, and more than 60% of the heat energy from nature and human-made settings is dissipated in the environment. Thermoelectric (TE) power generation is a reliable and environmentally friendly method for waste heat recovery as it enables solidstate direct conversion from heat to electricity without requiring any mechanical moving part.[1,2] The power outputs of TE generators (TEGs) are generally determined by the TE figures of merit (ZTs) of

materials, which are evaluated using the equation $ZT = S^2 \sigma T / \kappa$, where S, σ , κ , and T are the Seebeck coefficient, electrical conductivity, thermal conductivity, and absolute temperature, as well as the structural design of the module to optimize thermal transfer in the system.[3-7] Despite recent advancements in material efficiencies, the structural designs of TE legs and modules are affected by limited design flexibility within stereotypical planar structures. For real TE power generation applications, the module structures must sometimes be customized for integration with thermal systems or may require geometrical or heat-source-structure adjustments. [8] For example, tubular TEGs have been extensively studied in academia and industry to enhance fuel energy efficiencies by recovering automobile or industrial waste heat. [9-11] One important issue in such applications is the unavoidable temperature drop at the interface between the conventional planar TEG and exhaust gas pipe owing to unadaptable thermal contact, which significantly reduces the output power. Therefore, post-treatment by pressing the TEG onto the pipe with high force is required; however, this renders a heavy system.[12] These limitations in the module structures originate from underlying challenges with the bulk-scale material processes used to manufacture TEGs, such as top-down dicing, metallization, and soldering, www.advancedsciencenews.com

www.advenergymat.de

16146849, 2021, 20, Downloaded from https://ddvanced.onlinelibrary.viely.com/doi/10.1002/dem.m.02010190 by Pchang University Of Science, Wiley Online Library on [07092025]. See the Terms and Conditions (https://onlinelibrary.wiley.com/terms-and-conditions) on Wiley Online Library or rules of use; OA articles are governed by the applicable Creative Commons Licensea

owing to which precise engineering of structures for customization of TE legs and modules is impossible.

3D printing technology offers a revolutionary method to address these issues by computer-aided design and costeffective direct shaping of 3D bulk-scale TE legs and modules with optimized structures. [13-17] In recent years, there have been several research efforts to apply 3D-printing processes to TE materials and modules. Most of these studies focus on the production of Bi₂Te₃-based materials, which exhibit the highest ZTs near room temperature, necessitating for the expansion of printable TE materials that are operable at higher temperatures, for example, exhaust gases normally discharge at temperatures of 600-800 K.[12] Among the various TE materials, PbTe-based compounds are arguably some of the best in the temperature range of 500-800 K.[18] PbTe has a high-symmetry cubic crystal structure, complicated electronic band structures, and strong anharmonicity owing to the cationic disorder, resulting in a high Seebeck coefficient, high electrical conductivity, and low thermal conductivity. Moreover, recent studies have reported further enhancements in the ZTs of bulk PbTe materials from doping, nanostructuring, and band convergence.[18] In this study, we develop extrusion-based 3D printing of n-type and p-type PbTe materials and propose the design for a power-generating TE tube with customized tubular PbTe legs.

Extrusion of inks containing inorganic particles is the most widely utilized printing process for production of inorganic 3D objects because of its simplicity and affordable equipment price. In this process, the rheological properties of colloidal inks should be ensured to secure their 3D printability with continuous flow under dispensing and structural integrity after deposition.[19,20] Another important function of such inks is achieving sinterability of the printed inorganics during the post-sintering process while conserving material functionality with mechanical robustness. Inks with typical organic rheological modifiers, such as polymer-based resins are unsuitable for this purpose because such impurities sometimes cause retardation of sintering or undesired compositional changes in the final inorganic products after the post-sintering process.[14,21] Herein, we demonstrate that doping-induced surface charges of PbTe particles significantly improve the viscoelasticities of the inks without additives, enabling precise shape and dimension engineering of 3D bulk PbTe materials. Moreover, these impurity-free PbTe inks allow efficient sintering of the 3D-printed TE materials, with enhanced ZT values of up to 1.4 for the p-type and 1.2 for the n-type. Finally, a substrate-free self-sustaining power-generating TE tube was fabricated by assembling 3D-printed PbTe tubes. We characterized the power performance of the TE tube and used computational simulations to validate the proposed module structures, thus demonstrating the feasibility of 3D printing technology to design high-performance high-temperature-operable TEGs as customized structures.

2. Results and Discussion

2.1. Doping-Induced Viscoelasticity of PbTe TE Inks

The major challenge in this study was the development of impurity-free PbTe colloidal inks with viscoelasticities that

allowed 3D printability. One possible solution to this challenge is to induce strong surface charges in PbTe particles without using organic rheological modifiers. When the interparticle interactions among inorganic particles is repulsive and the electrostatic barrier against particle aggregation is sufficiently high, the colloid is kinetically stable, which guarantees continuous flow of inks during dispensing.[22,23] Moreover, the rheological properties of colloids are strongly dependent on the particle charges via the electroviscous effect. [23] The electrostatic barrier surrounding the charged particles contributes to increased energy dissipation during the flow of the liquid medium, consequently increasing both the viscosity and elasticity of the colloids. Further, over a wide range of concentrations, these effects promote particle network formation by electrostatic interactions among the charged particles, thereby exhibiting the desired viscoelasticities of inks for extrusion-based 3D printing. Our group demonstrated that the addition of Sb₂Te₄²⁻ chalcogenidometallate anions significantly enhances the viscoelasticities of colloidal inks of BiSbTe-based particles by negative charging of the particle surfaces. [13,15,22] However, these inorganic anions are not universally applicable to diverse classes of TE materials since the use of such inorganic additives may cause composition changes and doping in the final inorganic products after post-sintering, thus jeopardizing the expected TE performance. Herein, we observed that electronic doping induces strong surface charges of the PbTe particles in colloids via the imbalance of surface charges from atomic substitution, significantly improving the colloidal stabilities of particles and the staticstate viscoelasticity of the inks.

Figure 1a illustrates the extrusion-based 3D printing of nand p-doped PbTe colloidal inks to produce PbTe TE materials with defined shapes. Doped PbTe particles were synthesized by mechanical alloying in the presence of Na for p-type and Sb for n-type doping. The X-ray diffraction (XRD) patterns of the synthesized particles (Figure S1, Supporting Information) correspond to that of the reference bulk PbTe (Joint Committee on Powder Diffraction Standards, JCPDS # 01-072-6645) without any peaks for the impurities. The surface states of the particles were characterized by their ζ -potentials, demonstrating the surface charges of colloidal particles. Here, the ζ -potentials indicate the electrokinetic potential in a colloid. Undoped PbTe particles exhibit almost neutral surface charges with a ζ -potential of 6.19 mV (Figure 1b and Figure S2, Supporting Information). In contrast, the ζ -potential results of Na-doped and Sb-doped PbTe particles clearly show that they are negatively and positively charged, respectively. With increase in the Na doping content from 0.5% to 1.5% in PbTe particles, the ζ -potential progressively decreased from -8.87 to -27.8 mV. Further, the ζ -potential of Sb-doped PbTe particles increase from 13.5 to 29.9 mV with increase in the doping content from 0.5% to 1.5%. These results show that the surface charging of PbTe particles is induced by electronic doping with Na or Sb. Such doping-induced surface charging can be attributed to charge imbalance created by substitution of Pb²⁺ atoms with Na⁺ or Sb³⁺ at the surfaces (Figure 1e). Assuming homogeneous doping, for the 1.5% doped PbTe, the surface density of the dopant exposed to the surface is 7.19×10^{16} atom m⁻², resulting in a calculated surface charge density of 1.15×10^{-2} C m⁻², similar to those of other stable colloidal particles, such as polystyrene-latex (PSL),[24]

16146840, 2021, 20, Downloaded from https://advanced.onlinelibrary.wiley.com/doi/10.1002/aemm.202100190 by Pohang University Of Science, Wiley Online Library on [07/09/2025]. See the Terms and Conditions (https://onlinelibrary.wiley.com/doi/10.1002/aemm.202100190 by Pohang University Of Science, Wiley Online Library on [07/09/2025]. See the Terms and Conditions (https://onlinelibrary.wiley.com/doi/10.1002/aemm.202100190 by Pohang University Of Science, Wiley Online Library on [07/09/2025]. See the Terms and Conditions (https://onlinelibrary.wiley.com/doi/10.1002/aemm.202100190 by Pohang University Of Science, Wiley Online Library on [07/09/2025]. See the Terms and Conditions (https://onlinelibrary.wiley.com/doi/10.1002/aemm.202100190 by Pohang University Of Science, Wiley Online Library on [07/09/2025]. See the Terms and Conditions (https://onlinelibrary.wiley.com/doi/10.1002/aemm.202100190 by Pohang University Of Science, Wiley Online Library on [07/09/2025]. See the Terms and Conditions (https://onlinelibrary.wiley.com/doi/10.1002/aemm.202100190 by Pohang University Of Science, Wiley Online Library on [07/09/2025]. See the Terms and Conditions (https://onlinelibrary.wiley.com/doi/10.1002/aemm.202100190 by Pohang University Of Science, Wiley Online Library on [07/09/2025]. See the Terms and Conditions (https://onlinelibrary.wiley.com/doi/10.1002/aemm.202100190 by Pohang University Of Science, Wiley Online Library on [07/09/2025]. See the Terms and Conditions (https://onlinelibrary.wiley.com/doi/10.1002/aemm.202100190 by Pohang University Of Science, Wiley Online Library on [07/09/2025]. See the Terms and Conditions (https://onlinelibrary.wiley.com/doi/10.1002/aemm.202100190 by Pohang University Of Science, Wiley Online Library on [07/09/2025]. See the Terms and Conditions (https://onlinelibrary.wiley.com/doi/10.1002/aemm.202100190 by Pohang University Of Science, Wiley Online Library (https://onlinelibrary.wiley.com/doi/10.1002/aemm.202100190 by Pohang University Of Science, Wiley Online Library (https://onlin

and-conditions) on Wiley Online Library for rules of use; OA articles are governed by the applicable Creative Commons License

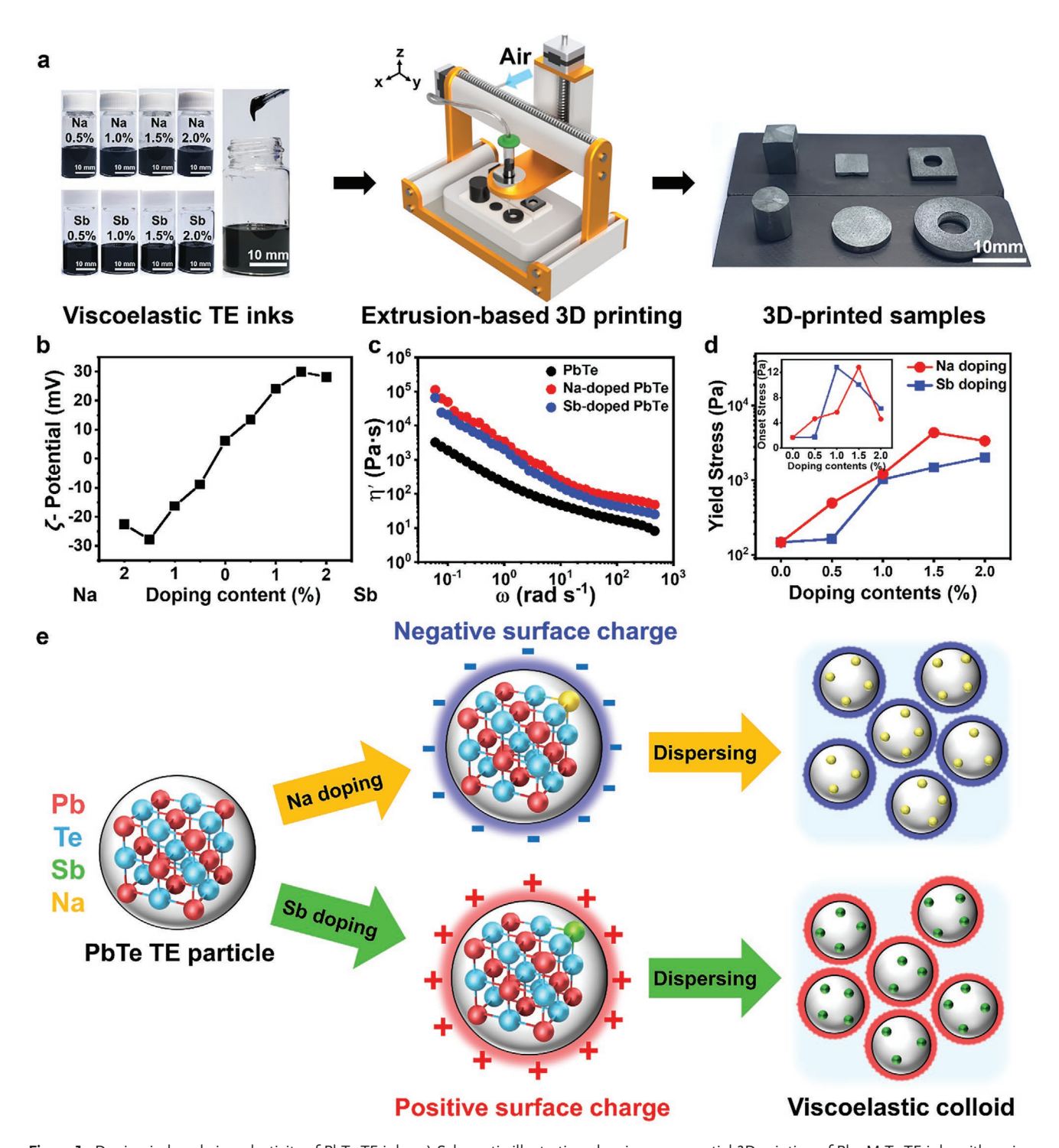


Figure 1. Doping-induced viscoelasticity of PbTe TE inks. a) Schematic illustration showing a sequential 3D printing of $Pb_{1x}M_x$ Te TE inks with various doping contents (M = Na or Sb, $0.5\% \le x \le 2\%$). Photograph showing the 3D-printed PbTe structures with various shapes such as cuboid, cylinder, plate, disk, perforated-plate, and tube. b) ζ -potential of the TE inks depending on the Na and Sb content. c) The dynamic viscosity (η ') curves of undoped, 1.5% Na-doped, and 1.5% Sb-doped PbTe inks. d) Yield stress of the inks consisting of $Pb_{1x}M_x$ Te (M = Na or Sb, $0.5\% \le x \le 2\%$). The inset indicates the onset stress of corresponding inks. e) Schematic illustration showing the doping-induced surface charges of Na- and Sb-doped PbTe particles generating viscoelastic colloids.

graphene oxide (GO), reduced GO (rGO),^[25] and nanoparticles.^[26] Several studies have reported similar phenomena for doped particles, for example, Sahu et al. reported that electronic

doping of TiO_2 nanoparticles with Cu^{2+} caused an increase in the ζ -potential owing to the charge imbalance between Ti^{4+} and Cu^{2+} and became stable electrostatically in dispersion. [27]

ADVANCED ENERGY MATERIALS

www.advancedsciencenews.com

www.advenergymat.de

16146849, 2021, 20, Downloaded from https://ddvanced.onlinelibrary.viely.com/doi/10.1002/dem.m.02010190 by Pchang University Of Science, Wiley Online Library on [07092025]. See the Terms and Conditions (https://onlinelibrary.wiley.com/terms-and-conditions) on Wiley Online Library or rules of use; OA articles are governed by the applicable Creative Commons Licensea

Further, Shkir et al. observed the increase of ζ -potentials in Ag doped PbS nanoparticles with increasing doping content and improved dispersion stability of doped PbS by electrostatic stabilization. [28] Additionally, in both case, the particles with 2.0% doping content exhibited slightly lower ζ -potentials compared with those of 1.5%. Since the solubilities of Na and Sb in the PbTe matrix do not exceed 1.5%, the reduction in ζ -potentials can be attributed to formation of dopant-related second phases, including nanoprecipitates (Figure S3, Supporting Information). [29,30] These precipitates may decrease the absolute values of the ζ -potentials by reducing the charge imbalances between Pb²⁺ and the dopant atoms.

Surface charging of the doped PbTe particles significantly improve the dispersion stabilities of inks by electrostatic repulsion, thereby enabling electrostatic stabilization of particles in colloids. As shown in Figure S4, Supporting Information, both Na- and Sb-doped PbTe particle inks maintain their phase stabilities for more than three days. Contrarily, sedimentation of the undoped PbTe particles were observed in the inks within a day after dispersion. Moreover, the doping-induced surface charges affect the fluidity of the ink and its printability (Video S1, Supporting Information). The flow properties were first studied by frequency-sweep rheological measurements of various inks (Figure 1c). It is noteworthy that the steady-state dynamic viscosities (0.06 rad s⁻¹) of n-type and p-type TE inks with 1.5% doping concentration are at least 20 and 34 times higher than that of pristine TE ink for the first measurement, respectively, thus confirming the excellent colloidal stabilities of doped particles by surface charging. The effects of doping concentration (Figure S5, Supporting Information) also suggest that while Na doping significantly affects both on the colloidal stability and flow property, irrespective of doping concentration, Sb doping enhances these properties only when the doping concentration is sufficient (>1.0%). In addition to observing the intrinsic natures of various inks in the 1st frequency-sweep test. we conducted stress and 2nd and 3rd frequency-sweep experiments to measure the flow properties of inks at a high shear stress of 300 Pa, similar to the 3D printing process condition.

The colloidal stabilities of various inks can be assessed not only by their dynamic viscosities but also by yield stresses obtained from the stress-sweep experiment. In Figure 1d and Figure S5, Supporting Information, it is clear that the yield stresses of inks increase with increasing doping concentrations, irrespective of the dopant type. Additionally, it is important to check the onset stress values in the stress-sweep experiment as shown in the inset of Figure 1d, because it is a key criterion for phase stability of the ink in the flow. However, unlike the yield stresses, it was observed that the onset stresses of doped inks decreased above a doping concentration of 1.5%, indicating that highly doped inks do not have high phase stabilities compared with the 1.0% inks. Nonetheless, these have high onset and yield stresses than the pristine TE ink.

In the 3D-printing process, it is essential to ensure colloidal and phase stabilities of inks, and a high degree of structural recovery for good integrity of the 3D-printed samples. Therefore, we conducted the 3rd frequency sweep with the same conditions as the 1st test to assess the thixotropic properties of various inks. In Figure S5, Supporting Information, it is noted that the pristine and 0.5% n-type doped inks exhibit

poor structural recovery, while the others show reasonably good viscosity regain even after application of a high shear stress of 300 Pa.

2.2. 3D Printing of Doped PbTe TE Materials

The 3D printability of the undoped and doped PbTe inks was comparatively explored by 3D-stacking tests to evaluate 3D-structure retention after ink deposition (Figure 2a and Figure S6, Supporting Information). [22] The layers were printed individually using the computer-aided design (CAD) models to produce the 3D structure. The undoped PbTe ink showed poor 3D-structure retention for deposition, as predicted by the rheological properties, where the 3D structure collapsed after deposition of the 5th layer. Contrarily, the doped PbTe inks showed good structural retention with sharp cuboidal edges up to the 50th layers. Moreover, the line width of the printed layers is uniformly, 230 µm (Figure 2b), the height and width of the 3D architecture can be defined using the number of printed layers. We demonstrated these capabilities by 3D-printing of cuboid-, cylinder-, plate-, disk-, perforated-plate-, and tube-shaped 3D samples with various lateral and vertical dimensions from 1 to 20 mm, which exactly matched the predesigned shapes and dimensions. Moreover, under the optimized printing conditions, we could 3D-print the square-shaped samples with the smallest lateral dimension of 2 mm × 2 mm (Figure S7a, Supporting Information), of which TE properties at room temperature was identical to those of 10 mm × 10 mm sample (Figure S7b, Supporting Information).

The as-3D-printed objects were dried and heat-treated at 1073 K under N2 atmosphere. For effective sintering of PbTe, Te powder of 5 wt% was added to the PbTe inks, which did not affect the 3D printability of inks. The Te powder is important for avoiding undesired Te deficiency in the final product from evaporation of Te during sintering. The XRD patterns of the sintered n-type and p-type PbTe materials (Figure 2c and Figure S8, Supporting Information) correspond to that of the cubic PbTe reference (JCPDS # 01-072-6645). Moreover, upon heat treatment, the liquified Te that melt at 450 °C could contribute to liquid-phase sintering and subsequent densification of samples having large grains with sizes of several tens of micrometers, as observed in the scanning electron microscopy (SEM) images (Figure 2d,e, and Figure S9,S10, Supporting Information) and densities (Figure S11, Supporting Information). The sintered samples printed from ink without excess Te had grains with sizes of several micrometers and multiple microscale pores among the grains (Figure S12, Supporting Information). The effective sintering of 3D-printed doped PbTe materials causes significant volume shrinkage in all the samples. However, this effect was highly reproducible given the doping type and content. Typically, the shrinkage is about 80% laterally and vertically, enabling to scale 3D products before printing.

2.3. TE Properties of 3D-Printed PbTe Materials

The remarkable sinterability and controlled doping in the 3D-printed PbTe materials are clearly reflected in their excellent

16146840, 2021, 20, Downloaded from https://advanced.onlinelibrary.wiley.com/doi/10.1002/aenm.202100190 by Pohang University Of Science, Wiley Online Library on [07/09/2025]. See the Terms

conditions) on Wiley Online Library for rules of use; OA articles are governed by the applicable Creative Commons

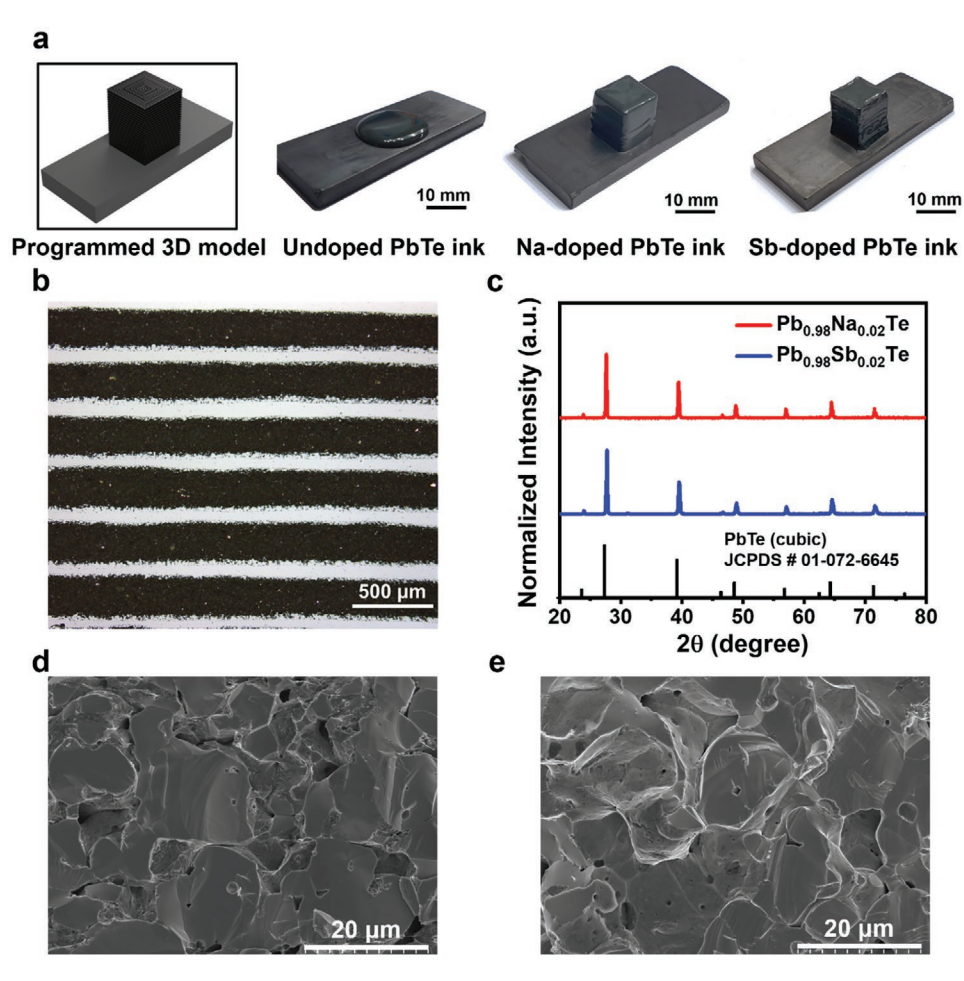


Figure 2. 3D printing of doped PbTe TE materials. a) Photographs showing the 3D stacking behaviors consisting of the doped and undoped PbTe inks. b) Optical microscopy image showing the printed lines of $Pb_{0.98}Sb_{0.02}Te$ ink. c) XRD pattern of 3D-printed $Pb_{0.98}Na_{0.02}Te$ and $Pb_{0.98}Sb_{0.02}Te$ samples. The vertical lines indicate the peaks corresponding to bulk cubic PbTe (JCPDS: 01-072-6645). d,e) SEM image of 3D-printed d) $Pb_{0.98}Na_{0.02}Te$ and e) $Pb_{0.98}Sb_{0.02}Te$ sample.

TE properties. The maximum ZT values of the p- and n-type samples were 1.4 at 700 K and 1.2 at 750 K, respectively (Figure 3a,e). It is noteworthy that these maxima observed for the 3D-printed PbTe samples are significantly larger than that of pure PbTe and comparable to the recently reported values of Na- and Sb-doped bulk materials synthesized by the traditional hot-pressing process or melting method (Figure S13, Supporting Information).^[29–36] Moreover, these values are among the highest the reported for TE materials fabricated by 3D printing with TE inks or pastes.^[13–17,37–39] The average ZT values at the mid-temperature range from 500 to 800 K are 1.05 for p-type and 0.82 for n-type PbTe (Figure S14, Supporting Information), confirming the applicability of 3D printing for mid-temperature waste heat recovery.

Depending on the doping content, carrier concentrations are clearly observed to increase in both material types (Figure S15, Supporting Information), demonstrating electronic doping by atomic substitution of Pb with Na or Sb. With the increase in the Na content from 0.5% to 2.0%, the hole concentrations increase from 4.78 \times 10 19 to 1.6 \times 10 20 cm $^{-3}$, and this range is in agreement with that observed for Na-doped PbTe bulk. $^{[29]}$ Moreover, the electron concentrations increase from 2.12 \times 10 19

to $4.56 \times 10^{19} \text{ cm}^{-3}$ with increase in the Sb doping content, consistent with that reported for Sb-doped PbTe bulk.[35] The reduction of carrier mobility with increase in doping content is understood by intensifying the carrier-carrier scattering with increasing carrier concentrations. Meanwhile, the mobilities of both p- and n-type PbTe are lower by a factor of 2 than the reported values for Na- and Sb-doped PbTe bulk. [29,35] This can be attributed to the unavoidable porosity of the 3D-printed PbTe materials, as observed in their microstructures. The sintering of 3D-printed PbTe materials was conducted under pressureless conditions without the precompaction process, which reduces the particle-particle contact area compared with the typical sintering process, resulting in creation of pores among the grains. Although the porosities of the current samples reduce the carrier mobilities, the macroscale pores are beneficial for enhancing ZT values because thermal transport is strongly affected by phonon scattering at the pore sites. For example, Lidorenko et al. theoretically predicted an increase of 30% in the ratio of electrical conductivity to thermal conductivity for porous SiGe alloys.^[40] Moreover, there are several reported instances of experimental evidence for the enhanced ZT values of porous TE materials.[41,42]

16146840, 2021, 20, Downloaded from https://advanced.onlinelbrary.wiley.com/doi/10.1002/aenm.202100190 by Pohang University Of Science, Wiley Online Library on [07/09/2025]. See the Terms and Conditions (https://onlinelbrary.wiley.com/doi/10.1002/aenm.202100190 by Pohang University Of Science, Wiley Online Library on [07/09/2025]. See the Terms and Conditions (https://onlinelbrary.wiley.com/doi/10.1002/aenm.202100190 by Pohang University Of Science, Wiley Online Library on [07/09/2025]. See the Terms and Conditions (https://onlinelbrary.wiley.com/doi/10.1002/aenm.202100190 by Pohang University Of Science, Wiley Online Library on [07/09/2025]. See the Terms and Conditions (https://onlinelbrary.wiley.com/doi/10.1002/aenm.202100190 by Pohang University Of Science, Wiley Online Library on [07/09/2025]. See the Terms and Conditions (https://onlinelbrary.wiley.com/doi/10.1002/aenm.202100190 by Pohang University Of Science, Wiley Online Library on [07/09/2025]. See the Terms and Conditions (https://onlinelbrary.wiley.com/doi/10.1002/aenm.202100190 by Pohang University Of Science, Wiley Online Library on [07/09/2025]. See the Terms and Conditions (https://onlinelbrary.wiley.com/doi/10.1002/aenm.202100190 by Pohang University Of Science, Wiley Online Library on [07/09/2025]. See the Terms and Conditions (https://onlinelbrary.wiley.com/doi/10.1002/aenm.202100190 by Pohang University Of Science, Wiley Online Library on [07/09/2025]. See the Terms and Conditions (https://onlinelbrary.wiley.com/doi/10.1002/aenm.202100).

conditions) on Wiley Online Library for rules of use; OA articles are governed by the applicable Creative Commons

www.advancedsciencenews.com www.advenergymat.de

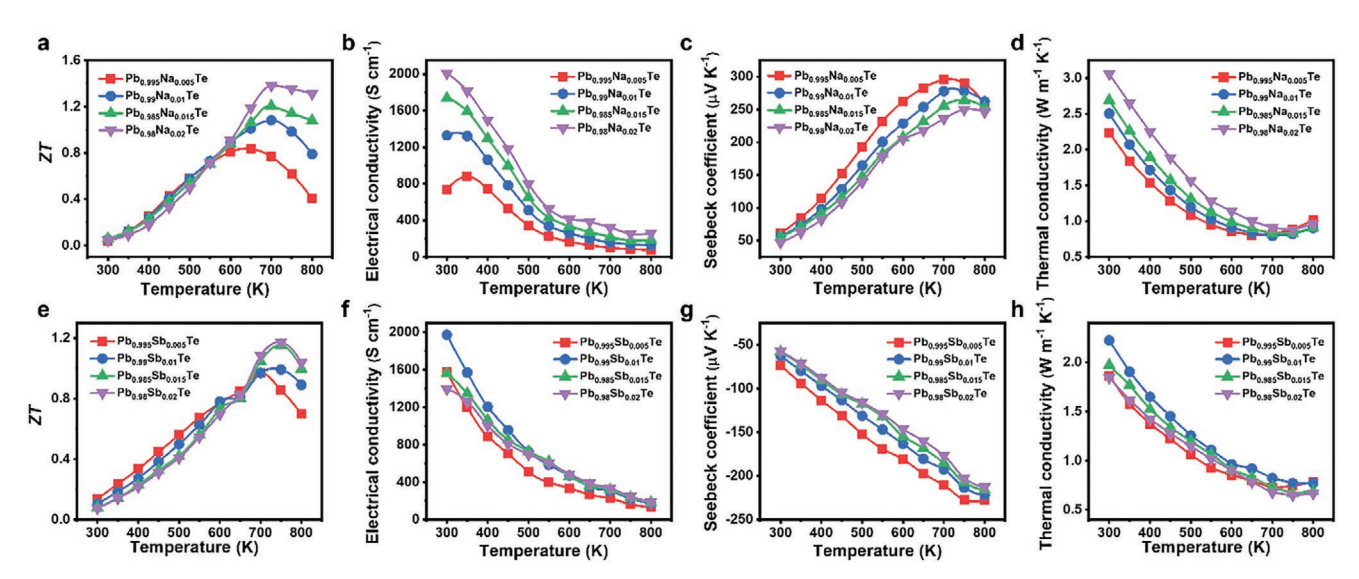


Figure 3. TE properties of the 3D printed PbTe samples. a–d) Temperature-dependent a) ZT, b) electrical conductivity, c) Seebeck coefficient, and d) thermal conductivity of the 3D-printed Na-doped PbTe. e–h) Temperature-dependent e) ZT, f) electrical conductivity, g) Seebeck coefficient, and h) thermal conductivity of the 3D-printed Sb-doped PbTe.

The temperature dependences of the electrical and thermal properties of the Na- and Sb-doped PbTe samples were characterized for 300-800 K. The magnitudes of the electrical conductivities for both types are of the order of 104-105 S m-1 at room temperature (Figure 3b,f), which are consistent with the reported values for doped PbTe bulk materials. Moreover, the electrical conductivities of both types were observed to clearly increase with increase in the doping content. The highest electrical conductivities at room temperature were around 2000 S m⁻¹ for 2% Na doping and 1% Sb doping, which are comparable to the reported values. In the case of the Sb-doped sample, the conductivity slightly decreases as the doping content increases at room temperature owing to carrier mobility reduction.[30,35] Meanwhile, the absolute Seebeck coefficients obtained for both types range from 50 to 80 µV K⁻¹ at room temperature and increase with increasing temperatures (Figure 3c,g). The highest values of 295.3 µV K⁻¹ for p-type and -227.6 μV K⁻¹ for n-type materials were obtained at 0.5% Nadoped PbTe at 700 K and 0.5% Sb-doped PbTe at 800 K, respectively. The room temperature Pisarenko plots (Figure S16, Supporting Information) shows that Seebeck coefficients of Na-doped PbTe are in two-band model, including a flattened curve of S owing to band convergence of heavy and light valence bands. Meanwhile, the Seebeck coefficients of Sb-doped PbTe agree with the curve of the single-band model. These electrical behaviors observed in both p- and n-type 3D-printed samples are consistent with the behaviors of reported PbTe without resonant state in the density of states. The highest power factors measured were 18.3 µW cm⁻¹ K⁻² for p-type 2% Na-doped sample at 650 K and 12.6 μ W cm⁻¹ K⁻² for n-type 1% Sb-doped sample at 550 K (Figure S17,S18, Supporting Information).

The temperature dependences of thermal conductivity for the Na- and Sb-doped PbTe (Figure 3d,h) show negative trends in the range from room temperature to 700 K. Above 700–750 K, slight increases were observed in both types, which can be attributed to the increased bipolar effect. Meanwhile, the thermal

conductivity of Na-doped PbTe increases with doping content, while that of 2% Sb-doped PbTe is lower than those of the 1% and 1.5% doped samples. The minimum thermal conductivities of the p- and n-type samples were 0.80 W m⁻¹ K⁻¹ at 1% Na-doped at 700 K and 0.65 W m⁻¹ K⁻¹ at 2% Sb-doped at 750 K. These minima are significantly lower than that of doped bulk crystalline PbTe, suggesting phonon scattering at the pore sites.

The lattice thermal conductivity (k_1) is calculated by subtracting electronic thermal conductivity (ke) from thermal conductivity. The electronic thermal conductivity relies on the Wiedemann-Franz law $k_e = L\sigma T$, where L is the Lorentz number, calculated by the equation of $L = 1.5 + \exp(-|S|/116)$. [43] As expected, the lattice thermal conductivity decreased as doping content increased at 650-700 K by enhancing impurity defect scattering (Figure S17,S18, Supporting Information). Moreover, it was clearly observed that the suppression of lattice thermal conductivities 1.5% and 2% doped samples at high temperatures, which indicates the suppression of bipolar conductivities by increasing the concentration of majority carriers. The lowest lattice thermal conductivity marked 0.54 W m⁻¹ K⁻¹ for 2% Na-doped PbTe at 700 K and 0.27 W m^{-1} K⁻¹ for 2% Sb-doped PbTe at 700 K. These extremely low values can be understood by considering the lower densities of the 3D-printed samples than bulk values and resulting multi-scale porosities, which can scatter phonons in the wide range of wavelengths.[44] For the quantitative estimation, the lattice thermal conductivities of 100% dense samples were predicted from the measured values of the 3D-printed samples by the effective medium equation of $k_1 = k_h(2-2\Phi)/(2+\Phi)$, where k_h and Φ are the lattice thermal conductivity of host materials and the porosity, respectively. The estimated lowest values (Figure S19, Supporting Information) were 0.67 W m⁻¹ K⁻¹ for 2% Na-doped PbTe and 0.41 W m⁻¹ K⁻¹ for 2% Sb-doped PbTe, being in the similar range of the reported values.[29,35]

We further investigated the thermal stability of the 3D-printed PbTe by the characterization of TE properties

16146840, 2021, 20, Downloaded from https://advanced.onlinelibrary.wiley.com/doi/10.1002/enm.202100190 by Pohang University Of Science, Wiley Online Library on [07/09/2025]. See the Terms and Conditions (https://onlinelibrary.wiley

conditions) on Wiley Online Library for rules of use; OA articles are governed by the applicable Creative Commons

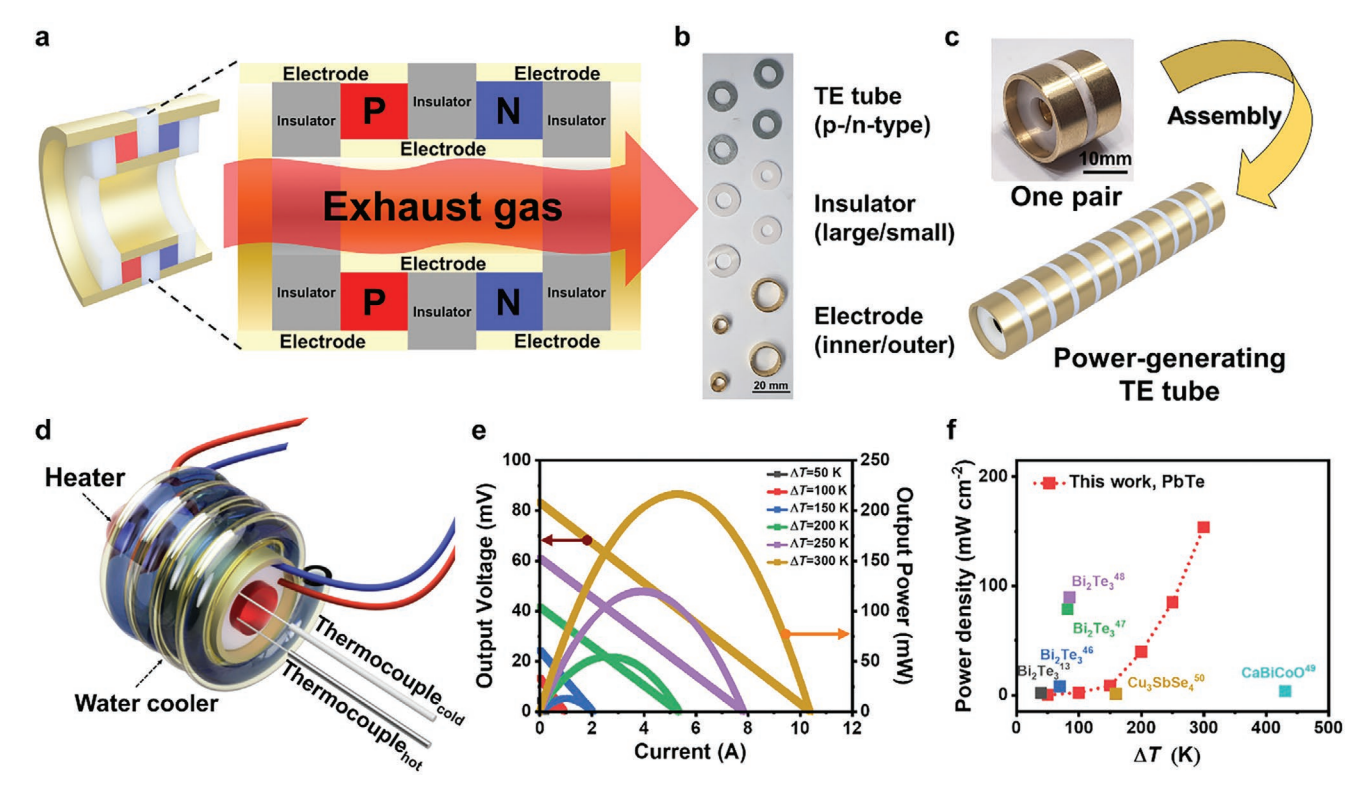


Figure 4. 3D printing of power-generating TE tube. a) Scheme showing the power-generating TE tube made of the 3D-printed p-type and n-type PbTe tubes at the front view. b) Photograph showing the components for the module assembly. c) Photograph of the fabricated power-generating TE tube chipping unipair of p-type and n-type PbTe legs and schematic model of a power-generating tube chipping ten pairs of TE legs assembled from the fabricated unit module. d) Illustration of the measurement set-up of output power of the TE tube. e) Output voltage and power of the TE tube under the different ΔT . f) Power density comparison of the current TE tube with the reported state-of-the-art tubular TEGs under the different ΔT .

through multiple heat cycles. Figure S20, Supporting Information shows the TE properties of the p-type Pb_{0.98}Na_{0.02}Te and n-type Pb_{0.98}Sb_{0.02}Te materials which exhibited the highest peak ZT values. In three cycles, the electrical conductivities, Seebeck coefficients, and thermal conductivities of both p-type and n-type PbTe were well preserved without degradation within the equipment error range, demonstrating the thermal stability of our samples.

2.4. 3D Printing of Power-Generating TE Tubes

The competitive TE properties and 3D printability achieved for high-temperature-operable PbTe materials enable the design of 3D free-form TE materials and modules beyond conventional planar structures. Herein, we propose a substrate-free power-generating TE tube design fabricated with 3D-printed PbTe tubes, which can be utilized directly as exhaust pipes through which hot fluids flow. This skeleton-type design of a TEG does not require processing for joining or customizing the TEG with a heat source, such as an exhaust gas pipe, thus rendering the entire power generation system light and simple. More importantly, our design provides the most effective means for heat transfer from high-temperature fluid flow through a tube to a TEG because there are no thermal resistive layers between the hot fluid and TE legs, such as a ceramic substrate in the TEG and pipes made of ferrous alloys.

Figure 4a–c illustrate the design of the proposed power-generating TE tube. Considering the 3D printability and TE properties, one pair of 2% Na-doped p-type and 2% Sb-doped n-type PbTe tubes of thickness 2 mm, outer diameter 14.2 mm, and inner diameter 8.2 mm were 3D printed (Video S2, Supporting Information) and used to fabricate the module with Cu tubular electrodes and ceramic filler tubes. The tubes were laterally assembled using Ag and ceramic adhesive pastes. The fabricated module resistance was 7.8 m Ω , which is higher than the expected value based on material properties; this is indicative of the contact resistance between the TE legs and Ag adhesive. Nevertheless, this resistance is in the range of those obtained with the reported typical planar modules. [45]

The output power values of the TE tube were measured by heating the inside of the tubular module with a cartridge heater having an identical outer diameter as the inner diameter of the TEG. The outer surface of the TEG was cooled with a water-circulating cooler (Figure 4d, Figure S21, Supporting Information). The measurement set-up of power performance was built in a vacuum chamber. Upon heating the hot side of the TEG from 300 to 747 K, the cold side temperature slowly increased to a maximum of 447 K (Figure S22,S23, Supporting Information). Although the cold side temperature did not remain at room temperature, the temperature difference thus created, that is, 400–800 K was optimal for the current 3D-printed TE materials according to their temperature-dependent TE properties. As the temperature difference increased, the output voltage increased

www.advancedsciencenews.com

www.advenergymat.de

16146840, 2021, 20, Downloaded from https://advanced.onlinelibrary.wiley.com/doi/10.1002/aenm.202100190 by Pohang University Of Science, Wiley Online Library on [07/09/2025]. See the Terms and Conditions

on Wiley Online Library for rules of use; OA articles are governed by the applicable Creative Commons License

almost linearly and output power increased quadratically, achieving a maximum output voltage of 83.2 mV and power of 216.3 mW at a temperature difference of 300 K (Figure 4e, Figure S23, Supporting Information). Furthermore, the maximum power density of 153.7 mW cm⁻² was significantly larger than those of reported tubular TEGs (Figure 4f). [13,46–50]

We further measured the power-generating performance of the TE tube under passive cooling, where the Cu foam heatsink was used for cooling the cold side of the TEG (Figure S24a, Supporting Information). Porous metallic foams have a very high cooling capacity under the convection flow due to their high surface to volume ratio. Moreover, they have mechanical flexibility, thus being suitable for cooling the curved surfaces.^[51] In our measurement, the power-generating tube was wrapped with a Cu foam heatsink for passive cooling under natural convection. Upon heating, the temperature difference increased gradually, and the maximum temperature difference of circa 250 K was created across the TEG when the hot-side temperature was at 800 K (Figure S22, Supporting Information). These temperature differences were at least ≈80% of those created by the active water-circulating cooler, showing the effectiveness of Cu foam heat sink for cooling. As the temperature difference increased, the output voltage and power increased with increasing the temperature differences (Figure S24b, Supporting Information). Moreover, the generated output power by passive cooling merged into the same line into the output power obtained by the active cooling (Figure S25, Supporting Information), demonstrating the reliability of our TEG and measurement. The slight deviation could be attributed to the

different properties of the materials in the different operating temperature ranges.

The thermal stability of the TEG was investigated by monitoring the changes in the output voltage and the module resistance over time while maintaining temperature difference at 200 K. As manifested in Figure S26, Supporting Information, the module resistance and output voltage did not change over 6 h, which clearly demonstrates the durability of our power-generating tube.

To further validate our tubular TEG design, we developed a 3D finite element model (FEM) that allowed calculating the temperature and power output in TEGs when hot exhaust fluid flow through the tube (Figure 5a). The contact resistance of 8.13 m Ω cm 2 obtained from the fabricated TE tube was assumed for the calculation to fit the module resistance. The calculated electrical output voltages and powers in the powergenerating TE tube showed good agreement with the experimental values (Figure 5a). Additionally, we compared the power generation of the TE tube with a typical tubular TEG design in which the ring-shaped TE legs mounted on a ceramic pipe, under the same environmental conditions (Figure 5b). For this calculation, the identical volume of TE legs and height of whole system were considered. Interestingly, at 800 K of hot fluid, the hot side temperature in the TE tube increased up to 743 K, while the significant temperature drop of ≈200 K was observed in the typical tubular TEG model (Figure 5c). Since the heat transfer rate is reciprocally proportional to the thermal resistance, this result indicates the minimal thermal resistance between the hot fluid and hot side of TE legs in the proposed

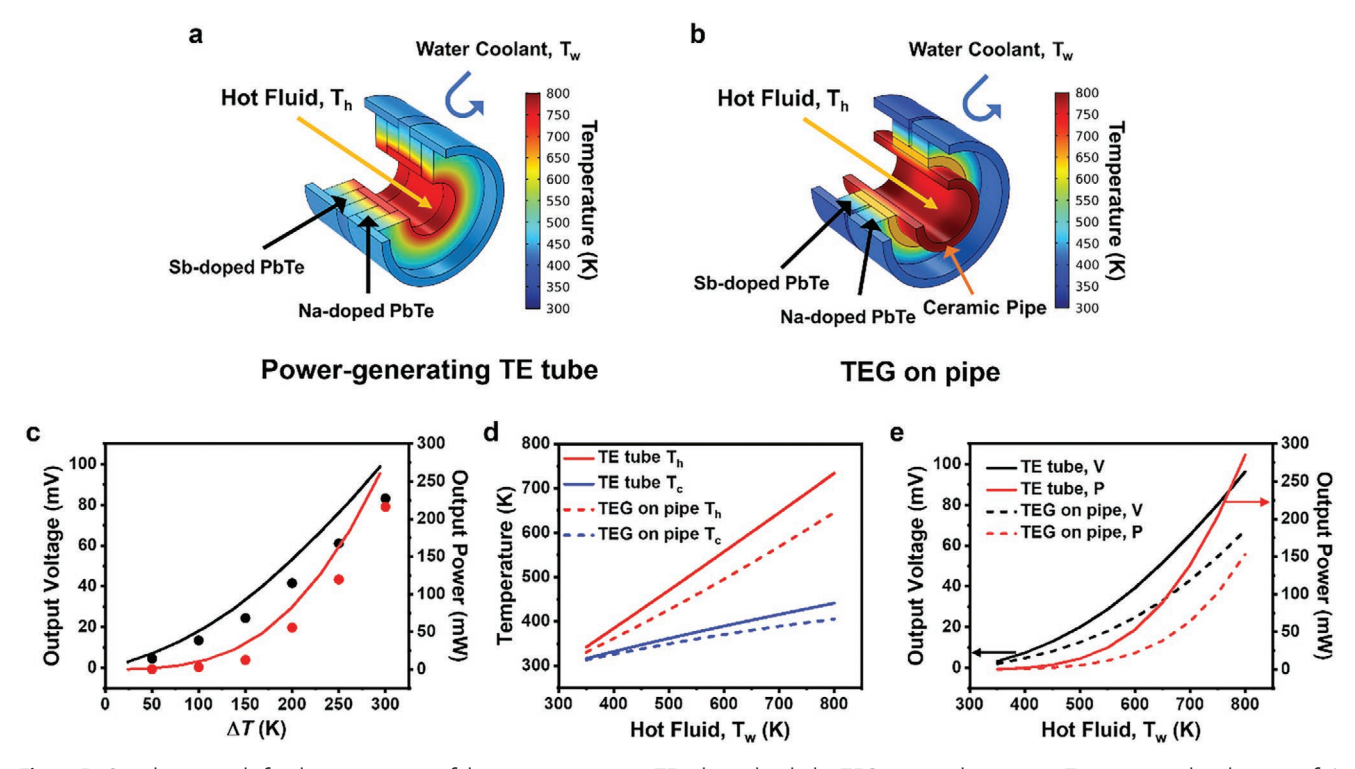


Figure 5. Simulation study for the comparison of the power-generating TE tube with tubular TEG mounted on a pipe. Temperature distributions of a) the TE tube and b) tubular TEG mounted on a ceramic pipe when the hot fluid at 800 K flow through. c) Calculated (line) and measured (dot) output voltage and power of the TE tube with respect to the temperature differences. d) Calculated temperatures of hot and cold sides, and e) output voltage and power of the TE tube (line) and tubular TEG mounted on a ceramic pipe (dash) with respect to the hot fluid temperature.

www.advancedsciencenews.com



16146840, 2021, 20, Downloaded from https://advanced.onlinelibrary.wiley.com/doi/10.1002/aemn.202100190 by Pohang University Of Science, Wiley Online Library on [07/09/2025]. See the Terms and Conditions (https://onlinelibrary.wiley.com/terms

and-conditions) on Wiley Online Library for rules of use; OA articles are governed by the applicable Creative Commons License

ADVANCED ENERGY MATERIALS

power-generating TE tube not having thermally resistive pipe. Accordingly, the calculated performance (Figure 5d) shows that the power-generating TE tube exhibit 1.8× larger output voltage and 2.8× higher output power than those obtained from the typical tubular TEG on a pipe, when the hot fluid at 800 K flow. Since the cold side temperatures increased with increasing the hot fluid temperatures in both simulation and experiment, we speculate that the introduction of an active cooling system with higher capacity would further increase the temperature gradient and power-generating performance.

3. Conclusion

In conclusion, we demonstrated the capability of the 3D printing-method for designing high-temperature-operable TE materials and system-adaptive customized power generators. We developed 3D-printable viscoelastic TE inks by engineering of the surface states of PbTe particles via atomic dopinginduced charge imbalance. Moreover, the rheological design of inks achieved their expected functionality of 3D printing, such as dimension and shape engineering of PbTe TE legs, which exhibited particularly high ZT values of 1.4 for the p-type and 1.2 for the n-type of the 3D-printed materials. We also realized power-generating TE tubes with customized tubular PbTe legs fabricated by 3D printing, and the design was validated to be the most effective and direct means of heat transfer from exhaust gases. Our approach therefore offers great potential for cost-effective processing to design high-performance customizable TE modules. In addition, For the industrialization of this technology, the corrosion by the exhaust gases is another potential issue. Exhaust gas usually contains reactive gases of O₂, CO, etc. In particular, O₂ gas can easily react with TE PbTe legs to form oxides phases such as PbO and TeO2, eventually degrading their functionality. To overcome this issue, recently, there have been several efforts to develop the technologies of anticorrosive coating for TE materials.^[52-55] For example, Brostow et al reported that the coating of high-temperature polymers for Bi₂Te₂-based TE materials significantly improves the service life of TE materials in corrosive environments.^[53] We believe that such anticorrosive coating technologies will accelerate the industrialization of the exhaust gas tubular TEGs. Meanwhile, we believe that this strategy of chemical design of the particles in colloidal inks could be easily transferred to other materials, thereby benefitting from 3D-printing techniques.

4. Experimental Section

Materials: Elemental lead (Pb, 99.95%, Alfa), elemental tellurium (Te, 99.999%, 5N+), elemental antimony (Sb, 99.999%, 5N+) and elemental sodium (Na, >95% Sigma-Aldrich) were used for high-energy ball milling. Glycerol (>99.5%, Sigma-Aldrich) were used for synthesis of ink.

Synthesis of All-Inorganic PbTe-Based Ink: The p-type TE powders with the stoichiometric composition of Pb $_{7x}$ Na $_x$ Te (x=0.05, 0.01, 0.015, and 0.02) were prepared by mechanical alloying using a high-energy ball milling process (Pulverisette 6; Fritsch) with a rotational speed of 450 rpm for 11 h. A zirconia milling jar (80 mL) was used with zirconia grinding balls ($\varphi=5$ mm) and the ball to powder ratio was 5:1 in weight. The n-type TE powders with the stoichiometric composition of Pb $_{7x}$ Sb $_x$ Te (x=0,0.05,0.01,0.015, and 0.02) were prepared by mechanical alloying

using a high-energy ball milling process (8000M Mixer/Mill, SPEX) under 5 h. they were ball-milled with stainless steel balls including two balls (φ = 12.7 mm) and four balls (φ = 6.35 mm). All procedure of ball milling was under N₂ atmosphere. The formation of PbTe-based alloys was confirmed by the XRD analysis (Figure S1, Supporting Information). A TE powder and 0.5 weight percent of tellurium powder were dispersed in glycerol of half mass weight of total powder, and the solution was mixed with a planetary centrifugal mixer (ARM-100, Thinky) for 30 min to fully homogenize the ink. ζ -potential data was collected using electrophoretic light scattering (ELS) analysis with a Nano-ZS of Malvern instrument. To get the electrophoretic mobility of individual particles, the PbTe inks were diluted by D.I. water and then sonicated more than 10 min, and then transferred to dip cell for measurement.

Rheological Properties of the Ink: The rheological properties of TE inks were evaluated by a rheometer (Haake MARS III, Thermo Scientific) equipped with a coaxial cylinder geometry sample holder. The frequency and stress sweep tests were performed as follows: the 1st frequency sweep was conducted in the frequency range of 0.05–300 rad s⁻¹ at a constant shear stress of 1 Pa, then the stress sweep experiment was done in the shear stress range of 0.005–300 Pa at a frequency of 1 rad s⁻¹ in order to measure the yield stress and onset stress that represent the force for colloidal structure disruption and the initial stress related to fluid instability, respectively. The 2nd frequency sweep was also conducted in the same frequency range of the 1st one at a constant shear stress of 300 Pa to impose high shear stress that is similar condition to 3D printing. The 3rd frequency sweep were taken under the same conditions of the 1st frequency sweep to assess the thixotropic properties of inks. All the measurements were carried out at 25 °C.

3D Printing Process: 3D printing of TE ink was performed using a home-built extrusion-based 3D printer with the control of temperature and pressure (Video S1, Supporting Information). The TE inks in a syringe barrel (5 mL), were deposited via metal nozzles with inner diameters varied from 210 to 920 μm . TE inks were printed on a graphite substrate by a structure designed by the software (Ultimaker Cura). Flow rate of TE ink was controlled by an air-powered dispenser. As-printed sample was dried at 373 K on a hot plate for 48 h and was annealed at 1023 K for 1 h 30 min and then 923 K for 3 h in a box furnace under N_2 atmosphere.

Materials Characterizations: XRD patterns were obtained using X'pert Pro (PANalytical) with a Cu K α X-ray source (wavelength of 1.5418 nm) equipped with an X'Celerator detector, operating at 40 kV and 30 mA. The scanning electron microscope images and elemental mapping images were collected by using a field-effect SEM (Nova-NanoSEM230, FEI and S-4800 Hitachi High-Technologies) operated at 10 kV. The optical microscopy images were obtained using an Olympus BX51M.

TE Properties of 3D-Printed Samples: The electrical conductivity and the Seebeck coefficients were measured simultaneous under Ar atmosphere at 50 K intervals over a temperature range of 300–800 K using a thermal analyzer (SBA458 Nemesis, Netzsch). The thermal conductivity (κ) was estimated using the relationship: $\kappa = \rho C_p D$, where ρ is the density, C_p is the specific heat capacity, and D is the thermal diffusivity. The thermal diffusivity was measured in the temperature range from 300 to 800 K by using a laser flash analyzer (LFA-457, Netzsch, Germany). The heat capacity C_p was determined from the measurements of Blachni κ by $C_p(k_{\rm B}/{\rm atom}) = 3.07 + 0.00047 (T/K-300)$ for lead chalcogenides. [56] The density was calculated by measuring the volume and weight. The carrier concentrations and mobilities were obtained at room temperature by using a Hall measurement system (HMS-8400, Lake Shore) with the magnetic field of ± 10 T.

Fabrication and Power Measurement of Power-Generating TE Tube: Large Cu tubes with a thickness of 6 mm, outer diameter 16.2 mm, and inner diameter 14.2 mm and small Cu tubes with a thickness of 6mm, outer diameter 8.2 mm, and the same size of Inner diameter with outer diameter of the cartridge heater were used as hot-side and cold-side electrodes in a TEG module, respectively. ZrO₂ tubes were used as insulating ceramic filler. The 3D-printed TE tubes with a thickness of 2 mm, outer diameter 8.2 mm, and inner diameter 14.2 mm were assembled lateral direction with Cu tubes and ceramic filler using Ag

ADVANCED ENERGY MATERIALS

www.advancedsciencenews.com www.advenergymat.de

paste (Pyro-Duct 597-A, Aremco) and ceramic adhesive paste. For measuring the TEG output power, the cartridge heater with a diameter of 6 mm was used as a heat source and its surface was coated with boron nitride layers with the thickness of 0.2 mm for electrical insulation. The water-circulating cooler was made to fit the outer diameter of TEG using Cu pipe. The whole measurement was carried out in a vacuum chamber to prevent oxidation. For the measurement of power generation, the TEG was connected to a Keithley 2400 through electrical feedthrough and the maximum power output (P) was calculated with relation: $P = V^2/4R$.

Numerical Simulation: A 3D finite element method (FEM) was implemented for coupled thermo-electrical model using commercial software COMSOL Multiphysics 5.4 to confirm the temperature distribution and generated electrical properties such as voltage and power in the TEG system. The TEG system consists of a heating part by hot fluid flowing tube, TE elements part, and a cooling part by water-circulating tube. For the heat dissipation from hot fluid flowing tube, fully developed laminar flow was assumed for a constant surface temperature along the tube, which is equivalent to specified convection coefficient, $h_{\rm f}$ (4463 W m⁻² K⁻¹), in case of the Hg working fluid. Likewise, the convection coefficient at the outer surface of the TEGs which is normal to radial direction, $h_{\rm c}$ (469 W m $^{-2}$ K $^{-1}$), is equivalent to forced cooling by 20 °C water flow in four coiled tube with diameter 3 mm. Moreover, natural convections by ambient air are considered at lateral side of the TEG system. For comparative simulations, TEG system using ring-shaped TE elements (with a thickness 2.75 mm, outer diameter 14.2 mm, and inner diameter 10.2 mm, equivalent to same system and electrode volumetric factor) mounted on a zirconia ceramic pipe (with an outer diameter 10.2 mm and inner diameter 8.2 mm) is considered under same heating and cooling boundary conditions. Thermal contact is neglected in all simulations.

Supporting Information

Supporting Information is available from the Wiley Online Library or from the author.

Acknowledgements

This work was supported by Samsung Research Funding Center of Samsung Electronics under Project No. SRFC-MA1801-05.

Conflict of Interest

The authors declare no conflict of interest.

Data Availability Statement

The data that support the findings of this study are available from the corresponding author upon reasonable request.

Keywords

 $\ensuremath{\mathtt{3D}}$ printing, doping, PbTe, power generators, thermoelectric materials

Received: January 19, 2021 Revised: March 23, 2021 Published online: April 15, 2021

- [1] L. E. Bell, Science 2008, 321, 1457.
- [2] F. J. DiSalvo, Science 1999, 285, 703.

- [3] G. J. Snyder, E. S. Toberer, Nat. Mater. 2008, 7, 105.
- [4] D. Rowe, G. Min, IEE Proc. Sci. Meas. Technol. 1996, 143, 351.
- [5] S. LeBlanc, Sustain. Mater. Technol 2014, 1, 26.
- [6] K. H. Lee, S.-i. Kim, H.-S. Kim, S. W. Kim, Acs. Appl. Energ. Mater. 2020, 3, 2214.
- [7] L. Yang, Z. G. Chen, M. S. Dargusch, J. Zou, Adv. Energy Mater. 2018. 8, 1701797.
- [8] B. Lee, H. Cho, K. T. Park, J. S. Kim, M. Park, H. Kim, Y. Hong, S. Chung, Nat. Commun. 2020, 11, 5948.
- [9] A. Schmitz, C. Stiewe, E. Müller, J. Electron. Mater. 2013, 42, 1702.
- [10] W. He, S. Wang, X. Zhang, Y. Li, C. Lu, Energy 2015, 91, 1.
- [11] F. Meng, L. Chen, Y. Feng, B. Xiong, Energy 2017, 135, 83.
- [12] Y. Zhang, M. Cleary, X. Wang, N. Kempf, L. Schoensee, J. Yang, G. Joshi, L. Meda, Energy Convers. Manag. 2015, 105, 946.
- [13] F. Kim, B. Kwon, Y. Eom, J. E. Lee, S. Park, S. Jo, S. H. Park, B.-S. Kim, H. J. Im, M. H. Lee, *Nat. Energy* 2018, 3, 301.
- [14] M. He, Y. Zhao, B. Wang, Q. Xi, J. Zhou, Z. Liang, Small 2015, 11, 5889.
- [15] S. E. Yang, F. Kim, F. Ejaz, G. S. Lee, H. Ju, S. Choo, J. Lee, G. Kim, S.-h. Jung, S. Ahn, H. G. Chae, K. T. Kim, B. Kwon, J. S. Son, *Nano Energy* 2020, 81, 105638.
- [16] J. Qiu, Y. Yan, T. Luo, K. Tang, L. Yao, J. Zhang, M. Zhang, X. Su, G. Tan, H. Xie, Energy Environ. Sci. 2019, 12, 3106.
- [17] N. Su, P. Zhu, Y. Pan, F. Li, B. Li, Energy 2020, 195, 116892.
- [18] Y. Xiao, L.-D. Zhao, npj Quantum Mater. 2018, 3, 55.
- [19] J. A. Lewis, Adv. Funct. Mater. 2006, 16, 2193.
- [20] T. D. Ngo, A. Kashani, G. Imbalzano, K. T. Nguyen, D. Hui, Compos. B Eng. 2018, 143, 172.
- [21] J.-H. Bahk, H. Fang, K. Yazawa, A. Shakouri, J. Mater. Chem. C 2015, 3, 10362.
- [22] Y. Eom, F. Kim, S. E. Yang, J. S. Son, H. G. Chae, J. Rheol. 2019, 63, 291.
- [23] J. Mewis, N. J. Wagner, Colloidal Suspension Rheology, Cambridge University Press, New York 2012.
- [24] K. Ohsawa, M. Murata, H. Ohshima, Colloid Polym. Sci. 1986, 264, 1005.
- [25] M. M. Gudarzi, Langmuir 2016, 32, 5058.
- [26] D. H. Gu, J. Lee, H. W. Ban, G. Lee, M. Song, W. Choi, S. Baek, H. Jeong, S. Y. Lee, Y. Choi, *Chem. Mater.* **2020**, *32*, 8662.
- [27] M. Sahu, P. Biswas, Nanoscale Res. Lett. 2011, 6, 441.
- [28] M. Shkir, M. T. Khan, I. M. Ashraf, S. AlFaify, A. M. El-Toni, A. Aldalbahi, H. Ghaithan, A. Khan, Ceram. Int. 2019, 45, 21975.
- [29] P. Jood, J. P. Male, S. Anand, Y. Matsushita, Y. Takagiwa, M. G. Kanatzidis, G. J. Snyder, M. Ohta, J. Am. Chem. Soc. 2020, 142 15464
- [30] H. Liu, Z. Chen, C. Yin, B. Zhou, B. Liu, R. Ang, Appl. Phys. A 2019, 125, 225
- [31] Y. Pei, A. LaLonde, S. Iwanaga, G. J. Snyder, Energy Environ. Sci. 2011, 4, 2085.
- [32] S. N. Girard, J. He, X. Zhou, D. Shoemaker, C. M. Jaworski, C. Uher, V. P. Dravid, J. P. Heremans, M. G. Kanatzidis, J. Am. Chem. Soc. 2011, 133, 16588.
- [33] K. Biswas, J. He, I. D. Blum, C. I. Wu, T. P. Hogan, D. N. Seidman, V. P. Dravid, M. G. Kanatzidis, *Nature* 2012, 489, 414.
- [34] H. S. Dow, M. W. Oh, B. S. Kim, S. D. Park, B. K. Min, H. W. Lee, D. M. Wee, J. Appl. Phys. 2010, 108, 113709.
- [35] T. Chen, K. Zhang, H. Wang, W. Su, F. Mehmood, T. Wang, J. Zhai, X. Wang, T. Huo, C. Wang, J. Mater. Chem. C 2020, 8, 1679.
- [36] G. Tan, C. C. Stoumpos, S. Wang, T. P. Bailey, L.-D. Zhao, C. Uher, M. G. Kanatzidis, Adv. Energy Mater. 2017, 7, 1700099.
- [37] C. Han, G. Tan, T. Varghese, M. G. Kanatzidis, Y. Zhang, ACS Energy Lett. 2018, 3, 818.
- [38] M. R. Burton, S. Mehraban, D. Beynon, J. McGettrick, T. Watson, N. P. Lavery, M. J. Carnie, Adv. Energy Mater. 2019, 9, 1900201.
- [39] M. R. Burton, S. Mehraban, J. McGettrick, T. Watson, N. P. Lavery, M. J. Carnie, J. Mater. Chem. A 2019, 7, 25586.



ADVANCED ENERGY MATERIALS

16146840, 2021, 20, Downloaded from https://advanced.onlinelibrary.wiley.com/doi/10.1002/aemm.202100190 by Pohang University Of Science, Wiley Online Library on [070/9/2025]. See the Terms

of use; OA articles are governed by the applicable Creative Commons

www.advancedsciencenews.com www.advenergymat.de

- [40] N. Lidorenko, O. Narva, L. Dudkin, R. Erofeev, *Inorg. Mater.* 1970, 6, 1853.
- [41] P.-H. Chang, M. S. Bahramy, N. Nagaosa, B. K. Nikolic, *Nano Lett.* 2014, 14, 3779.
- [42] H. Ning, G. D. Mastrorillo, S. Grasso, B. Du, T. Mori, C. Hu, Y. Xu, K. Simpson, G. Maizza, M. J. Reece, J. Mater. Chem. A 2015, 3, 17426.
- [43] H.-S. Kim, Z. M. Gibbs, Y. Tang, H. Wang, G. J. Snyder, APL Mater. 2015, 3, 041506.
- [44] H. Lee, D. Vashaee, D. Wang, M. S. Dresselhaus, Z. Ren, G. Chen, J. Appl. Phys. 2010, 107, 094308.
- [45] P. Jood, M. Ohta, A. Yamamoto, M. G. Kanatzidis, Joule 2018, 2, 1339.
- [46] G. Min, D. M. Rowe, Semicond. Sci. Technol. 2007, 22, 880.
- [47] A. Sakai, T. Kanno, K. Takahashi, H. Tamaki, H. Adachi, Y. Yamada, J. Electron. Mater. 2012, 42, 1612.
- [48] A. Sakai, T. Kanno, K. Takahashi, H. Tamaki, Y. Yamada, J. Electron. Mater. 2015, 44, 4510.

- [49] O. V. Merkulov, B. V. Politov, K. Y. Chesnokov, A. A. Markov, I. A. Leonidov, M. V. Patrakeev, J. Electron. Mater. 2018, 47, 2808.
- [50] Y. Liu, G. García, S. Ortega, D. Cadavid, P. Palacios, J. Lu, M. Ibáñez, L. Xi, J. De Roo, A. M. López, S. Martí-Sánchez, I. Cabezas, M.d.l. Mata, Z. Luo, C. Dun, O. Dobrozhan, D. L. Carroll, W. Zhang, J. Martins, M. V. Kovalenko, J. Arbiol, G. Noriega, J. Song, P. Wahnón, A. Cabot, J. Mater. Chem. A 2017, 5, 2592.
- [51] Y. Shi, Y. Wang, D. Mei, Z. Chen, IEEE Access 2018, 6, 43602.
- [52] P. Nieroda, K. Mars, J. Nieroda, J. Leszczyński, M. Król, E. Drożdż, P. Jeleń, M. Sitarz, A. Koleżyński, Ceram. Int. 2019, 45, 10230.
- [53] W. Brostow, I. K. Chen, J. B. White, Sustain. Energy Fuels 2017, 1, 1376.
- [54] W. Brostow, T. Datashvili, H. E. H. Lobland, T. Hilbig, L. Su, C. Vinado, J. White, J. Mater. Res. 2012, 27, 2930.
- [55] P. Wei, C.-L. Dong, W.-Y. Zhao, Q.-J. Zhang, J. Inorg. Mater. 2010, 25, 577.
- [56] R. Blachnik, R. Igel, Z. Naturforsch. B 1974, 29, 625.